PAPER

Measuring mesoscopic scales in complex fluids embedded with giant cylindrical micelles with diffusing wave spectroscopy micro-rheology

To cite this article: Antonio Tavera-Vázquez *et al* 2022 *J. Phys.: Condens. Matter* **34** 034003

IOP Publishing Journal of Physics: Condensed Matter
J. Phys.: Condens. Matter **34** (2022) 034003 (17pp) https://doi.org/10.1088/1361-648X/ac2c3e

Measuring mesoscopic scales in complex fluids embedded with giant cylindrical micelles with diffusing wave spectroscopy micro-rheology

Antonio Tavera-Vázquez[1], Natalia Rincón-Londoño[2], Ricky F López-Santiago and Rolando Castillo*

Instituto de Física, Universidad Nacional Autónoma de México, PO Box 20-364, 01000 Mexico City, México

E-mail: rolandoc@fisica.unam.mx

Received 14 August 2021, revised 27 September 2021
Accepted for publication 1 October 2021
Published 8 November 2021

Abstract

This review paper presents a procedure for measuring the mesoscopic scales in micellar solutions embedded with giant cylindrical micelles using the mean square displacement determined with a quasi-elastic multiple light scattering method (diffusing wave spectroscopy) and theory. The mesoscopic scales of interest are the micelles' total contour length, persistence and entanglement lengths, and the mesh size of the entangled micellar network. All of them depend on the physicochemical parameters of the solutions and determine the rheological behavior. We present an assessment of the whole procedure, the scattering experiments performance, the recovery of optical parameters, which includes dealing with the light absorption and its treatment, and how to develop the micro-rheology for obtaining the mesoscopic scales in these complex fluids.

Keywords: light scattering, diffusing wave spectroscopy, wormlike micelles, micro-rheology, light absorption, viscoelasticity

(Some figures may appear in colour only in the online journal)

1. Introduction

Many properties observed in fluid soft materials are related to the complex supramolecular structures embedded in them. They introduce a complex dynamics usually described with multiple characteristic lengths and time scales. The rheological response of these materials can be linear or non-linear depending on the applied stress. Usually, nonlinearity is a sign of structural rearrangement in the system by the applied stress or deformation. However, there is always a linear response regime for small enough applied strain or stress for systems close to thermodynamic equilibrium. One of the most important properties in this regime is the shear modulus, $G(t)$, which connects the deformation and flow of materials in response to applied stress $\sigma = \int_{-\infty}^{t} G(t-t')\dot{\gamma}\,\mathrm{d}t'$ [1]. Here, σ is the shear stress and $\dot{\gamma}$ is the shear rate. In the frequency domain, $G(t)$ can be transformed into the response to shear excitations characterized by the complex shear modulus $G^*(\omega) = \mathrm{i}\omega\int_0^{\infty} G(t)\mathrm{e}^{-\mathrm{i}\omega t}\,\mathrm{d}t$ that determines the stress induced on a material upon applying an oscillatory shear strain, γ, at a frequency ω. The complex shear modulus can be expressed as $G^*(\omega) = G'(\omega) + \mathrm{i}G''(\omega)$. The real part is the elastic (storage) modulus in phase with the applied γ. The imaginary part corresponds to the viscous (loss) modulus in phase with $\dot{\gamma}$. In contrast with simple

[1] Present address: Pritzker School of Molecular Engineering, The University of Chicago, Chicago, IL 60637, United States of America
[2] Present address: División de Ciencias e Ingenierías, Universidad de Guanajuato, León, México
* Author to whom any correspondence should be addressed.

liquids or solids, the shear modulus in soft materials exhibits a substantial time dependence; it can be in the range of milliseconds to seconds or even to minutes; consequently, soft materials are viscoelastic, i.e., they exhibit both a viscous and elastic response. Linear viscoelasticity properties are usually measured with rotational mechanical rheometers [2] in the frequency domain, probing macroscopic samples in the milliliter range, along a limited frequency range ($\omega \sim 10^{-1}$–50 rad s^{-1}), and with different deformation geometries depending on the extent of strain and the magnitude of shear modulus to be measured.

On the other hand, microrheological techniques, which essentially measure the same shear modulus, but with several advantages, are nowadays reliable to get useful structural and dynamic information in soft materials. Micro-rheology does not describe a particular technique. The general principle behind micro-rheology is to minimize the mechanical probe that deforms the medium, which could be a small particle, like a colloidal microsphere, and a modern technique to trace the particle probe movement. In particular, a colloidal particle is a delicate probe, which introduces the slightest possible perturbation in the structure and dynamics of delicate soft matter (thermal energies $\sim k_B T$, k_B is the Boltzmann's constant, T is absolute temperature). That combination allows the measurement of the rheological material properties at the micrometer and sub-micrometer scales. In contrast to what occurs with rotatory mechanical rheometers, the material's strain is virtually negligible during measurements due to the probes' small size. Particularly, this feature is useful in complex fluids, in which even small imposed strains can cause structural reorganization in those materials and, consequently, a change in the viscoelastic properties. The basic assumption in micro-rheology is that the surrounding medium's mechanical properties determine the micron-sized colloidal particles' motion dispersed within a fluid. Naturally, micro-rheology can be used to examine the linear response of complex fluids. Experimental methods fall into two classes depending on the forces operating on the probe particles [3, 4]. In passive microrheology, the material's properties are extracted from the motion of thermally fluctuating probes. During the last three decades, micro-rheological techniques have boomed for their ability to extract information at small lengths and time scales. Scaling down the probing devices as colloidal microspheres [5, 6] or microcantilevers made that possible when used as the sensors [7–9]. We find in this group particle tracking with video microscopy, diffusing wave spectroscopy (DWS), and extensions like multispeckle DWS [10]. In active microrheology [6], a probe is actively driven within the material, either in oscillatory or steady motion using optical tweezers, magnetic tweezers, or atomic force microscopy. In the case of DWS, it is possible to make an extension to measure the viscoelastic spectrum to high frequencies, $\omega \sim 10^6$ rad s^{-1}, that can provide an insight into fast relaxation times in complex fluids, which are out of the range for rotatory mechanical rheometry; although, also there are mechanical piezoelectric devices that can reach high frequencies [11]. In the case of colloidal probes, which are embedded in the complex fluid of interest, local trajectories are tracked along in response to stochastic thermal forces, similar to those observed in the well-known Brownian motion in simple liquids but now altered by the viscoelastic susceptibility of the liquid bulk. The mean square displacement (MSD, $\langle \Delta r^2(t) \rangle$) of these particles can be related to the viscoelastic spectrum $G^*(\omega)$ of the fluid by a generalization of the Stokes–Einstein equation, given by Mason and Weitz [12–14], as we will describe below.

In fluids embedded with self-assembled giant cylindrical micelles, also called wormlike micelles (WLMs), the capacity to reach high-frequencies by DWS provides a significant step forward for micro-rheology because it is an outstanding alternative to standard static scattering techniques, as small-angle neutron scattering (SANS) or small-angle x-ray scattering (SAXS) [15], to obtain structural information. DWS micro-rheology can estimate the most important characteristic lengths of major interest to understand the structure and dynamics of WLMs, using approximate relations coming from theory. For example, the total contour length of the micelles, L_C, their persistence length l_p, entanglement length, l_e, and the mesh size, ξ, of the entangled micellar network. In the mentioned scattering techniques, scattering spectra (neutron or x-ray scattering intensity vs wave vector, q) of WLM solutions are obtained and related to scattering spectra of theoretical models of assemblies of cylindrical micelles where polydispersity effects in size and diameter can be included. These scattering curves can give information about the apparent radius of gyration and apparent molar mass at the lowest q, and in some cases, the total contour length and micelle flexibility, given by l_p, in the intermediate q range, as well as the local structure at higher q as micelle diameter and the mass per length of the cylindrical micelle. SAXS and SANS have been able to determine the cylindrical nature of WLMs, and they have provided characteristic lengths for many WLM systems. However, complex facilities are needed to do the experiments, where the user must obtain beam-time and funds for traveling, as well as an elaborate data treatment is finally needed to extract the desired information. These requirements make these techniques not easy to use to develop systematic studies, like those needed to understand the whole picture of how the solution's physicochemical parameters affect the WLM's characteristic lengths. In contrast, in micro-rheology, standard light scattering equipment, which is commonly affordable in many laboratories, can give complementary information to scattering techniques that help understand the micellar structure and dynamics. Other techniques getting some of these characteristic lengths can be used as neutron spin echo [16, 17], birefringence measurements [18], and in some cases dynamic light scattering [19], but with limited success.

In solution, amphiphilic molecules self-assemble to form various supramolecular structures, the geometry of which can be spherical, cylindrical, lamellar, etc [20, 21]. The preferred geometry is fixed by the spontaneous curvature determined by the assembled aggregates' most effective packing. The organization within these structures will depend on a complex interplay of molecular geometry, amphiphilic character, and charge of all the involved entities in the supramolecular structures. The interplay can be modified by several factors, namely, surfactant concentration, cosurfactants, hydrotope salts, and pH,

temperature, and ionic strength of the media (salt addition). The preferred interfacial curvature optimizes the system energetically, but it does not account for entropy effects. At low concentration, below the critical micelle concentration (CMC), i.e., below micelles are formed, entropy favors a uniform dissolution of the amphiphile in the solvent, so that self-assembly and aggregation are negligible. Above the CMC interaction dominates, and entropy effects are reduced. Consequently, the number of aggregates, usually spherical, sharply increases. Afterward, amphiphiles form cylindrical micelles with moderate spontaneous curvature. In these structures, energy is optimized when the curvature is uniform everywhere, forming long linear structures (giant cylindrical micelles or WLMs). However, entropy introduces a degree of randomness through the bending of the cylindrical micelles, which adds conformational entropy like the configurational entropy of polymeric chains and certain topological defects in the form of end-cap and/or branch junction points. These two defects are introduced by forming regions with differing local curvatures that sustain different energetic penalties. The overall entropic gain associated with end-caps is greater than that of branch points. Although topological defects' appearance introduces an entropy gain, the type of defect that dominates the system is set by the amphiphile spontaneous curvature. If the scission energy, E_{sc}, of a cylindrical micelle (the energy required to create two end-caps from an infinite cylinder) is large enough, then the linear micelles may become very long and entangled at a relatively low total volume fraction of surfactant. Lowering the scission energy shortens the total contour length, L_C, of the linear micelles and entropy increases by increasing the number of micelles in the micelle solution. This competition between energy and entropy mainly determines L_C. The distance between entanglement points along a WLM will be denoted by l_e. On the other hand, branch junction points increase the number of possible configurations, enabling percolation and the formation of extended micellar networks, which leads to a multi-connected rather than an entangled network of cylindrical micelles. Although, transitions between linear and branched micelles are unusual. When salt is added to ionic surfactants, the electrostatic repulsions between headgroups are screened, inducing a linear growth because the scission energy increases. However, after a maximum, salt addition suggests a decrease in micellar size. Above the CMC, the micellar system is in the dilute regime up to the overlap concentration; the semidilute regime lies between the overlap concentration and a concentration where the network mesh size, ξ, is larger than the WLM persistence length, l_p. Here, the linear rheology is dominated in a good approximation by a single relaxation time at low and intermediate frequencies, as in a Maxwellian fluid, i.e., a single relaxation mode dominates, and the viscoelastic modulus that can be written as: $G(t) = G_o\, e^{-t/\tau}$ [22, 23]. G_o denotes the elastic modulus, which is related to the micellar mesh size, and τ is the relaxation time. The reptation-reaction model [24] for WLMs proposes that the relaxation time is the geometric mean of two characteristic times: micellar breaking and recombination, τ_b, and micelle reptation, τ_R, where τ_b must be much smaller than τ_R. Therefore, linear rheology at low frequencies in WLMs is mainly dominated by reptation and reversible breaking and recombination between them. At high frequencies, other relaxation modes appear. Micro-rheology can contribute to estimating the characteristic lengths of the WLM network due to its capability to obtain $G^*(\omega)$ at high frequencies and approximate relations coming from theory. At time scales shorter than WLM breakage time that corresponds to high frequencies, the Maxwellian stress relaxation processes are fundamentally frozen; WLMs behave like semiflexible polymer chains. Then, stress relaxes first dominated by the Rouse–Zimm modes and later by internal relaxation of Kuhn segments. $G^*(\omega)$ exhibits, at those frequencies, a power-law behavior, $|G^*| \sim \omega^{\nu}$, with the exponent $\nu \sim 5/9$ in the Rouse–Zimm regime, which shifts to $\nu \sim 3/4$, where the internal bending modes of Kuhn segments dominate. That change occurs at a frequency ω_o ($\omega_o \approx k_B T/8\eta_s {l_p}^3$; η_s is the solvent viscosity) [11] that corresponds to the shortest relaxation time in the Rouse–Zimm spectrum. From ω_o coming from the slope change in $|G^*(\omega)|$, l_p can be obtained, and the other characteristic lengths can be evaluated. The WLM network mesh size can be obtained in the loose entanglement regime with $\xi \cong (Ak_BT/G_o)^{1/3}$, where the prefactor $A = 9.75$ is a recent correction [25]. In the same way, l_e can be calculated using $l_p = \xi^{5/3}/{l_p}^{2/3}$ [26]. From ${G''}_{min}/G_o \cong (l_e/L_C)^{0.8}$, the total contour length can be estimated by incorporating breathing and high-frequency Rouse modes. The exponent in this equation is a correction given by Granek [27]. Here, ${G''}_{min}$ is a local minimum of $G''(\omega)$ after the first crossing between $G'(\omega)$ and $G''(\omega)$. The ratio of the entanglement length to the persistence length can also be obtained, $\alpha_e = l_e/l_p$, and it is helpful to determine if the system is in the loose ($\alpha_e > 2$) or tight entanglement regime ($\alpha_e < 1$) [25].

At low and intermediate frequencies, Maxwell-like behavior is followed by most of the WLM solutions, i.e., a single relaxation dominates, where the moduli follow a semicircle $[G''(\omega) - 0]^2 + \left[G'(\omega) - G_o/2\right]^2 = \left[G_o/2\right]^2$ that is known as the Cole–Cole plot. However, at higher frequencies, the crossover to other relaxation modes appear (breathing) and express themselves as a minimum in this plot, so the subtle departures from exponential behavior in this crossover region are easily seen in this Cole–Cole representation. One crucial point of the reptation-reaction model [24] is that this dip's height is directly related to the average number of entanglements along the WLM chain. There are examples of WLM systems where that semicircle is followed at low frequencies, but at higher frequencies, there is no minimum, or it is not deep enough. Here, the mentioned equations are not expected to work for multiple reasons such as, τ_b is not much smaller than τ_R, or there is a mechanism that does not allow the solution to reach equilibrium [28]. When these flaws do not occur, the reptation-reaction model has shown to be adequate to describe the behavior of WLM systems, as determined from experiments [29, 30] and simulations [25–27, 31].

DWS extends the analytical power of dynamic light scattering to the limit of multiple scattering events [32, 33]; some of the first examples to study WLM solutions can be found in references [30, 34, 35]. It is based on two fundamental assumptions: (1) the diffusion approximation of light, where the light intensity is carried by scattered photons due to the embedded

probe particles in the fluid to be studied along many paths to the detector, with step sizes of the order of the transport mean free path, l^*, and (2) an average on scattering events over many particles, instead of considering just individual events. Nevertheless, DWS can provide unique information on particle motion on short time scales because coherent light is scattered from a large number of colloidal particles, where each particle moves only a small fraction of a wavelength. Cumulative change in the path length produces an interference speckle pattern at the detector. At a low concentration (particle volume fractions $\phi \sim 0.01$–0.02), interparticle interactions can be considered to be negligible. Therefore, DWS allows us to examine a fluid forming a turbid suspension due to the embedded particles, and their motion can be probed at short length scales from $\sim$1 nm up to $\sim$1 μm, by measuring a time autocorrelation function of the scattered light intensity, which can be related to the MSD of these probe particles. However, it is essential to mention that the fluid under investigation must not absorb light in a first approximation before the microsphere addition. Weitz and Pine first suggested this correction but without presenting analytical results [32, 33]. To deal with this problem, different methods are used. In Sarmiento-Gómez and co-workers' procedure [36], the measured field autocorrelation function must include a correction term, l^*/l_a, that quantifies the loss of light by absorption effects. l_a is the so-called absorption length, which is equivalent to the inverse of the absorption coefficient, μ_a, and l^* is the transport mean-free path that is the length over which the direction of light propagation is randomized. The absorption of light is given as an exponential attenuation, cutting off the longest paths. For recovering l^* and l_a from the fluid of interest, several procedures can be followed. In reference [36], the authors used the inverse adding doubling (IAD) method [37–39], where just three measurements need to be performed, namely, total reflectance, total transmittance, and collimated transmittance of the incident light on the fluid with probes. The recovered optical parameters are: $\mu'_s = 1/l^*$, $\mu_a = 1/l_a$, and the anisotropy factor g (cosine average of the scattering angles due to all the scattering events in the turbid medium). These measurements are done using an integrating sphere. Hajjarian and Nadkarni [40] simulated light propagation in any medium with arbitrary optical properties, using a computational intensive Monte-Carlo ray tracing algorithm. They derived a numerical solution to relate the intensity correlation function with the MSD for glycerol and water solutions, where the optical properties of the mixtures were tuned by adding various concentrations of TiO_2 particles and carbon light-absorbing nano-powder. In all cases, Mie's theory was used to calculate the optical properties, and measurements were developed in backscattering geometry, which limited the frequency range of the rheological modulus ($\omega < 20$ rad s^{-1}). The results go in the right direction but present large deviations when compared with the mechanical rheological data. Zhang *et al* [41] developed a method that instead of comparing the optical properties of the non-adsorbing sample with another sample whose l^* is known, they determine the static optical properties of the sample in a particular commercial instrument, in forward and backscattering, to perform DWS measurements. The method relies on a comparison with an extensive set of calibration measurements. l^* and l_a are obtained with an accuracy $\sim$8% and 14%, respectively. They tested their approach on suspensions of polystyrene latex spheres where absorption is introduced by adding different amounts of green food dye. They did not compare their micro-rheological results with mechanical rheological measurements neither reported using the technique for a structured complex fluid.

Our group has developed a procedure for measuring the mesoscopic scales in micellar solutions embedded with giant cylindrical micelles using the MSD determined with a quasi-elastic multiple light scattering method and theory of these micelles. Here, we present an assessment of the whole procedure, namely, how the scattering experiments are performed with DWS, to overcome the challenges of recovering the optical parameters, to treat absorption in the case that systems absorb light, to develop the micro-rheology for obtaining the mesoscopic scales in these complex fluids. Afterward, we discuss how the information given by these mesoscopic scales in a fluid embedded with cylindrical micelles can improve our understanding of the rheological behavior of these fluids.

2. Theory behind the quasi-elastic multiple light scattering method

2.1. Diffusing wave spectroscopy without light absorption

In DWS, there are two different allowed experimental geometries: total transmission and backscattering. The multiply scattered light loses information of its origin and propagation direction after traveling a distance $\sim l^*$, within a planar sample with a light path $L \gg l^*$. This l^* is related to the mean free path, l, which is the distance traveled among every scattering event $l^* = l/\langle 1 - \cos\theta \rangle$. Here, θ is the single-event scattering angle, and $\langle \ldots \rangle$ represents an ensemble average upon all realizations of scattering events. For small particles, near the Rayleigh scattering limit, when $k_o a \ll 1$ ($k_o = 2\pi/\lambda$ is the wave vector of the incident light, a is the radius of the particles and λ is the wavelength of light), single-particle scattering is isotropic, and the direction of light is randomized after one scattering event ($l^* = l$). For larger particles in the Mie scattering limit, the scattering reaches a maximum in the forward direction. There are necessary several scattering events, on average, to randomize in the direction of propagation ($l^* > l$). Each beam emerges from the sample with a phase that depends on its total path length s. Assuming independence of light paths, the normalized field autocorrelation function can be written as [32, 33]:

$$g^{(1)}(t) = \frac{\langle \mathbf{E}(0)\mathbf{E}^*(t) \rangle}{\left\langle |\mathbf{E}|^2 \right\rangle} = \int_0^\infty P(s) \exp\left[-\frac{1}{3} k_0^2 \left\langle \Delta r^2(t) \right\rangle \frac{s}{l^*} \right] \mathrm{d}s, \tag{1}$$

where $\mathbf{E}(t)$ is the scattered electric field, $P(s)$ is the path distribution function of scattered photons. A diffusion equation of the energy density describes the transport of light, which is like Fick's law. For calculating $P(s)$, the diffusion equation must obey the initial and boundary conditions to ensure no net flux

of diffusive photons entering the sample. For details, see reference [33]. The resulting equations can be solved using Green's functions techniques, as discussed by Carslaw and Jaeger [42]. The most used geometry in the laboratory is the transmission one, which is useful to probe motion over length scales much shorter than λ. For the case of a sample with parallel plane faces and with uniform illumination of a plane-wave beam, the autocorrelation function can be written as a function of the MSD of probe particles as:

$$g^{(1)}(t) = \frac{\frac{L/l^*+4/3}{\alpha^*+2/3}\left[\sinh(\alpha^* x) + \frac{2}{3}x\,\cosh(\alpha^* x)\right]}{\left(1+\frac{4}{9}x^2\right)\sinh\left(\frac{L}{l^*}x\right) + \frac{4}{3}x\,\cosh\left(\frac{L}{l^*}x\right)}, \quad (2)$$

with $x = \sqrt{k_0^2\langle\Delta r^2(t)\rangle}$ and $\alpha^* = z_0/l^*$. The value $z_0 \sim l^*$, although numerical values are insensitive to the exact choice of z_0, since $L \gg z_0$. A different choice of z_0 would affect only the first few steps in a random walk that consists of many steps. Backscattering geometry can also be used [43]. The MSD of probe particles can then be determined by collecting their scattered light from a single speckle during an extended period (40 to 180 min), evaluating the time-averaged intensity auto-correlation function.

2.2. Diffusing wave spectroscopy including light absorption

Recently, a method was developed to circumvent absorption issues in DWS, deriving a correction to the theory [36]. As mentioned above, Weitz and Pine first suggested this correction, although they did not present an actual proof of the method [32, 33]. They pointed out that absorption exponentially attenuates light paths according to their path length, cutting off the longest paths. Therefore, if $P(s)$ is the path length distribution in the absence of absorption, the path length distribution in the presence of absorption must be $P(s)\exp(-s/l_a)$, as derived from first principles in [36]. Then, equation (1) can be rewritten as:

$$g^{(1)}(t) = \int_0^\infty P(s)\exp\left[-\left(\frac{1}{3}k_0^2\left\langle\Delta r^2(t)\right\rangle + \frac{l^*}{l_a}\right)\frac{s}{l^*}\right]\mathrm{d}s. \quad (3)$$

The effect of absorption represents a time delay in the time axis by l^*/l_a. As for the conventional DWS, a diffusion equation for the energy density is necessary to get an analytical expression for $g^{(1)}(t)$. Therefore, an absorption term must be included to get the correct path distribution function of scattered photons. A diffusion equation can be derived from the radiative transport equation, with an absorption-independent diffusion coefficient [44], by considering a nearly isotropic light distribution and assuming that $l_a \gg l^*$ [45, 46]. For the transmission geometry, following reference [36], the equation for the field autocorrelation function is:

$$g^{(1)}(t) = \frac{\frac{\left(1+\frac{4}{9}\eta^2\right)\sinh\left(\frac{L}{l^*}\eta\right)+\frac{4}{3}\eta\,\cosh\left(\frac{L}{l^*}\eta\right)}{\sinh(\alpha^*\eta)+\frac{2}{3}\eta\,\cosh(\alpha^*\eta)}\left[\sinh(\alpha^* x_a) + \frac{2}{3}x_a\,\cosh(\alpha^* x_a)\right]}{\left(1+\frac{4}{9}x_a^2\right)\sinh\left(\frac{L}{l^*}x_a\right) + \frac{4}{3}x_a\,\cosh\left(\frac{L}{l^*}x_a\right)}, \quad (4)$$

where $\eta = \sqrt{3l*/l_a}$ and $x_a = \sqrt{k_0^2\langle\Delta r^2(t)\rangle + \eta^2}$. Equation (4) seems to be more complicated than its counterpart with no absorption. Nevertheless, when $l_a \to \infty$, we recover the equation (2). The measured time-averaged light intensity autocorrelation function $g^{(2)}(t)$ can be related to the electric field autocorrelation function $g^{(1)}(t)$ through the Siegert relation [33]. The theoretical ensemble average involved in $g^{(1)}(t)$ can be switched to a temporal average when ergodic systems are assessed. In conclusion, when light absorption in the fluid of interest cannot be neglected, the MSD of the microspheres can be obtained by numerical inversion of equation (4). However, there are some technical restrictions. One must guarantee that $9 \leqslant L/l^* \leqslant 25$ [36, 47], which refers to the number of scattering events in the sample. If the relation L/l^* is too small, diffusing light beams decreases; on the contrary, if L/l^* is large, the possibility for colloidal particle interactions among them increases [43]. Besides, it would be convenient that $l_a/l^* \geqslant 30$ [36]. It refers to whether the absorption is too much. If it is not obeyed, light paths can be attenuated more than needed, producing a deficiency of scattering events, and consequently, an absence of diffusing light beams.

2.3. Micro-rheology

The method starts at the standard Langevin description for a particle immersed in a complex fluid undergoing Brownian motion, modified to include viscoelastic effects, using a time-dependent memory function, the Maxwellian fluid time-dependent memory function, which accounts for both energy loss and storage upon deformation. The MSD of the colloidal particles can be related to the continuum viscoelastic properties of the system through the generalized Stokes–Einstein equation relationship proposed by Mason and Weitz [12, 14, 48] in the Laplace domain:

$$\tilde{G}(z) = \frac{k_B T}{\pi a z\left\langle\Delta r^2(z)\right\rangle}, \quad (5)$$

a is the particle radius, and z is the Laplace frequency. Equivalently, in the Fourier domain, $G^*(\omega)$ can be given [14, 48]. For both formulas, it is assumed: (a) the complex fluid is treated as a continuum medium around the spherical particle. This argument is valid when the length scales of the structures giving rise to the elasticity are much smaller than the particle's radius. (b) The Stokes relation for the drag, ζ^*, in the fluid can be

used to determine a complex viscosity, η^*, ($\zeta^*(\omega) = 6\pi a\eta^*(\omega)$) overall frequencies, which is related to the complex modulus, $\eta^*(\omega) = G^*(\omega)/\mathrm{i}\omega$. The equation relating the complex modulus of a viscoelastic fluid with the unilateral Fourier transform ($\Im_u$) of the probe particle MSD can be written as:

$$G^*(\omega) = \frac{k_\mathrm{B}T}{\pi a\,(\mathrm{i}\omega)\,\Im_u\left\{\langle\Delta r^2(t)\rangle\right\}}. \tag{6}$$

Different authors have followed several procedures to determine the unilateral Fourier transform. One method develops locally around the frequency of interest using a power law and evaluating the logarithmic derivative [14]. Here, $G'(\omega) = |G^*(\omega)|\cos(\pi\alpha(\omega)/2)$, $G''(\omega) = |G^*(\omega)|\sin(\pi\alpha(\omega)/2)$, and

$$|G^*(\omega)| \approx \frac{k_\mathrm{B}T}{\pi a\,\langle\Delta r^2(1/\omega)\rangle\,\Gamma(1+|\alpha(\omega)|)}, \quad \text{with}$$
$$\alpha(\omega) \equiv \frac{\mathrm{d}\,\ln\langle\Delta r^2(t)\rangle}{\mathrm{d}\,\ln\,t}|_{t=1/\omega}. \tag{7}$$

Another procedure is related to the relation between the dynamic relaxation modulus $G(z)$ and the dynamic compliance modulus $\gamma = \int_{-\infty}^{t} J(t-t')\dot{\sigma}\,\mathrm{d}t'$. $J^*(\omega) = \mathrm{i}\omega\int_0^\infty J(t)\,\mathrm{e}^{-\mathrm{i}\omega t}\,\mathrm{d}t$, and $J^*(\omega)G^*(\omega) = 1$, and therefore equation (5) can be expressed as [49]:

$$J(z) = \frac{1}{zG(z)} = \left[\frac{\pi a}{k_\mathrm{B}T}\right]\langle\Delta r^2(z)\rangle, \text{ or } J(t) = \left[\frac{\pi a}{k_\mathrm{B}T}\right]\langle\Delta r^2(t)\rangle. \tag{8}$$

Thus, from the $\langle\Delta r^2(t)\rangle$ data, numerically evaluated data points (t_i, J_i) can be obtained, or $J(t)$ can be obtained by fitting a model curve to the experimental values of $\langle\Delta r^2(t)\rangle$ vs t. For recovering $G^*(\omega)$, the following formula is used [50]:

$$\frac{\mathrm{i}\omega}{G^*(\omega)} = \mathrm{i}\omega J(0) + (1-\mathrm{e}^{-\mathrm{i}\omega t_1})\frac{[J_1 - J(0)]}{t_1} + \frac{\mathrm{e}^{-\mathrm{i}\omega t_N}}{\eta} + \sum_{k=2}^{N}\left(\frac{J_k - J_{k-1}}{t_k - t_{k-1}}\right)\left(\mathrm{e}^{-\mathrm{i}\omega t_{k-1}} - \mathrm{e}^{-\mathrm{i}\omega t_k}\right). \tag{9}$$

One different procedure is to employ $z \to \mathrm{i}\omega$ (analytic continuity) in equation (6), to obtain the real and complex components of $G^*(\omega)$, where $\langle\Delta r^2(t)\rangle$ could be obtained by fitting a model curve to the experimental values of $\langle\Delta r^2(t)\rangle$ vs t obtained from the numerical inversion of the intensity correlation functions. For the case of particles immersed in WLM solutions, the experimental MSD curves can be best fitted to a model curve suggested by Bellour *et al* [51]:

$$\langle\Delta r^2(t)\rangle = 6\delta^2(1-\mathrm{e}^{-\left(\frac{D_\mathrm{o}}{\delta^2}t\right)^{\gamma'}})^{\frac{1}{\gamma'}}\left(1+\frac{D_\mathrm{m}}{\delta^2}t\right). \tag{10}$$

Here, $6\delta^2$ measures the plateau of $\langle\Delta r^2(t)\rangle$ vs t curve (a graph of this curve is in figure 4), D_o, and D_m are the diffusion coefficients for particles in the solvent at infinite dilution and at long times, respectively, and γ' is a parameter that accounts for the broad spectrum of relaxation times at the plateau. It is common for doing the fittings to leave to δ, D_m, D_o, and γ' as free parameters. In this function, we observe three different motion regimes shared by all micellar solutions reported in the literature, no matter the concentration or the temperature. At short times, there is a regime where $\langle\Delta r^2(t)\rangle$ is almost a linear function of time; $\langle\Delta r^2(t)\rangle = 6D_\mathrm{o}t$, where D_o is the diffusion coefficient. At intermediate times, $\langle\Delta r^2(t)\rangle$ remains constant for a given time interval (a plateau). Here, the model was built to describe the motion of Brownian particles harmonically bound around a stationary mean position, as a consequence $\langle\Delta r^2(t)\rangle = 6\delta^2(1-\mathrm{e}^{-\left(\frac{D_\mathrm{o}}{\delta^2}t\right)})$, where the particle's amplitude of the motion, the cage size δ, is related to the elastic modulus G_o ($\delta^2 = k_\mathrm{B}T/6\pi aG_\mathrm{o}$), which does not depend on ω. At those intermediate times, particles are bound to their mean position, on time scales smaller than the micellar system's longest characteristic time, $\tau_\mathrm{M} = \eta_\mathrm{m}/G_\mathrm{o}$ [24]; here, η_m is the long-time viscosity of the system. At the inflection point, $6\delta^2$ is the value of the mean square displacement. In a WLM fluid, the cage where particles are momentarily trapped fluctuates due to the breaking/reptation process. Then, at longer times, $\langle\Delta r^2(t)\rangle$ is once again a linear function of time, $\langle\Delta r^2(t)\rangle = 6D_\mathrm{m}t$; as a consequence, it was proposed that $\langle\Delta r^2(t)\rangle = 6\delta^2(1-\mathrm{e}^{-\left(\frac{D_\mathrm{o}}{\delta^2}t\right)})\left(1+\frac{D_\mathrm{m}}{\delta^2}t\right)$. However, this last expression did not correctly describe the plateau onset time dynamics because the microspheres' dynamics exhibit a vast time relaxation spectrum. This led to including the parameter γ' to give equation (10) [51].

3. Quasi-elastic multiple light scattering experiments

a. Samples. In these experiments, rectangular optical glass cuvettes with different optical path lengths, from 1 to 5 mm (Starna Cells, Inc. or Hellma GmbH & Co.), are used to place the suspensions to be measured in the scattering experiments where the micellar system and the microspheres are added. Depending on the experiment, the microspheres can be functionalized to change their surface's charge or chemistry to make the suspension more stable. They must have a low polydispersity (Bangs Laboratories), and it is common to use polystyrene microspheres ($\sim$ 800 nm). The larger the difference of index of refraction between microspheres and the solvent, the better. It is a good practice for obtaining the actual weight concentration to perform thermogravimetric measurements evaporating the solvent with a thermogravimetric analyzer (TGA, TA Instruments).

b. Diffusing wave spectroscopy. Our DWS setup is a homemade instrument (see figure 1(a)) [30]. A 514.5 nm laser beam (1) (Ar^+, Spectra-Physics, or Melles Griot) pass through a spatial filter (2), where it is expanded, and subsequently, a large pupil eliminates the external part of the Gaussian beam to approximate the beam to a plane wave (4). The beam shines the sample in a thermally stabilized bath (5) and (6). The scattered light passes through an achromatic doublet (7) and through a crossed polarizer (8) to increase the autocorrelation response. Next, the light is collected by an optical fiber (OZoptics Inc.) (9) and detected by two photomultipliers (Thorn EMI) (10). The autocorrelation function is obtained by a Digital

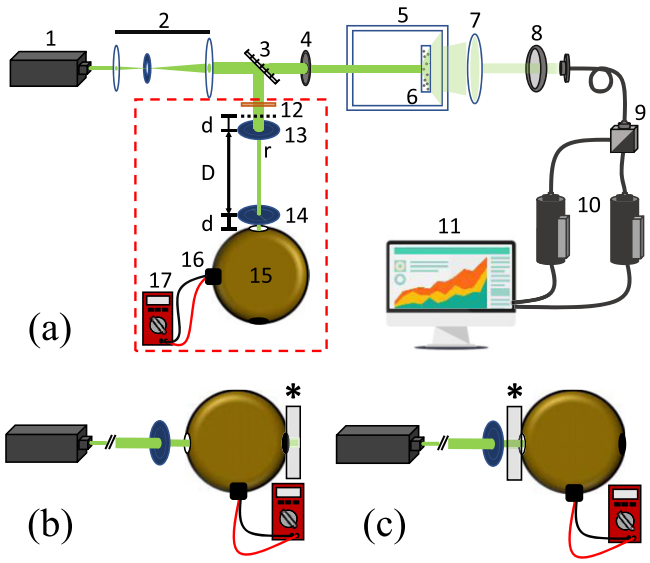

Figure 1. (a) DWS experimental setup. The branch within the red dashed frame is used to recover the samples' optical parameters (l^*, l_a, and g). Setup of the integrating sphere to obtain (b) M_R and (c) M_T. Laser light is sent to the sample to obtain the reflected or transmitted light. *Corresponds to the location of the sample to be analyzed.

Correlator (Flex 02-08D/C, USA) in cross-correlation mode, controlled with a computer (11). For determining the values of l^* and l_a, a mirror (3) is set next to the spatial filter to make use of the branch framed by a red dashed square in figure 1(a). We use an integrating sphere (Oriel, Newport) (15) [52]. Between the mirror and the integrating sphere, we set an optical filter and two diaphragms (13 and 14), separated at a fixed distance to obtain the input parameters for IAD. The light signal is detected by a photomultiplier tube (Hamamatsu Photonics, Japan) (16), connected to a voltmeter (17). After a numerical inversion procedure, the IAD method gives l^*, l_a, and the anisotropy factor g [36, 37, 53].

c. Inverse adding doubling (IAD) method. To recover the optical parameters l^* and l_a from the suspensions, we followed the procedure described in reference [36] using the IAD method [37–39]. In this method, a general numerical solution for a radiative transport equation is given through the following steps: (a) an educated guess for a set of the optical parameters is given. (b) The samples' reflection and transmission are estimated using the adding doubling method [54, 55]. (c) Transmittance and reflectance are compared with the experimental measurements. (d) If the match is not good enough, the set of optical parameters is modified using a minimization algorithm. The process is iteratively followed until a match with the experimental measurements is reached. The IAD method also considers several features experimentally challenging to assess, such as light lost out of the sample cell edges and non-linear effects in the integrating sphere measurements. We followed the experimental considerations and computational algorithms described in the literature and used the available open-source code [39, 53]. ***Collimated transmittance*:** a light beam is sent to the integrating sphere that goes first through an optical attenuator (12, in figure 1(a)) and then to the sample (black dashed line in figure 1(a)). According to simulation studies [53], diaphragm apertures (r), separations between the sample and the first diaphragm (d), both diaphragms (D), and from the second diaphragm to the integrating sphere (d) are crucial for obtaining proper measurements. Previous studies showed that for $D > 25$ cm, the results are good enough; in our case $D = 68$ cm. Both diaphragms must be as close as possible to the sample and the integrating sphere ($d = 5$ cm). The aperture should be approximately the same size as the original profile waist, $r = 0.15$ cm. Collimated transmittance is related to the Beer–Lambert law, which determines a logarithmic dependence between the collimated transmittance, M_U, of light through the sample, and the attenuation coefficient times the traveled distance within the sample, $M_U = I_i/I_0 = e^{-\mu l}$, where I_i is the intensity of the light beam with a sample, and I_0 is the intensity of the beam without sample. The coefficient of attenuation considers the attenuation due to scattering and absorption, namely $\mu = \mu_s + \mu_a = \mu_s + 1/l_a$. Where $\mu_s = \mu'_s/(1-g) = 1/(l^*(1-g))$. The term μ'_s is named the reduced scattering coefficient, which is a property incorporating the scattering coefficient μ_s and the anisotropy factor g. μ'_s describes photons' diffusion in a random walk step size (the transport mean free path, l^*); each step involves isotropic scattering (considered in the term $1-g$). This equation connects the mean free path of light with the transport mean free path. So, $g = \langle \cos\theta \rangle$, with θ the deflection angle due to each scattering event. ***Reflectance and transmittance*:** to measure total reflectance, M_R, and total transmittance, M_T, of light on and through the sample, respectively, with the integrating sphere, we used the equations [39]:

$$M_R \equiv r_{std}\frac{R\left(r_s^{direct}, r_s\right) - R(0,0)}{R\left(r_{std}, r_{std}\right) - R(0,0)},$$
$$M_T \equiv \frac{T\left(t_s^{direct}, r_s\right) - T_{dark}}{T(0,0) - T_{dark}}. \quad (11)$$

Each term in these equations is measured independently, according to figures 1(b) and (c), which shows just the elements within the framed branch of the experimental setup shown in figure 1(a). We used a diaphragm with an aperture ~ 4 mm. For reflectance (figure 1(b)), r_{std} is the reflectance value of the integrating sphere walls, $R(r_{std}, r_{std})$ is the reflection measurement for a standard sample, $R(r_s^{direct}, r_s)$ is the reflection measurement for the sample, and $R(0, 0)$ is the measurement of the intensity of light without sample when light is allowed to go out of the sphere. For transmittance (figure 1(c)), the sphere's back wall is never open (light that does not interact with the sample bounces around in the sphere). $T(0, 0)$ is the measurement of light intensity when the light strikes inside the sphere without sample, $T(t_s^{direct}, r_s)$ is the transmission measurement through the sample, and T_{dark} is the measurement of the intensity of light with the entrance port blocked.

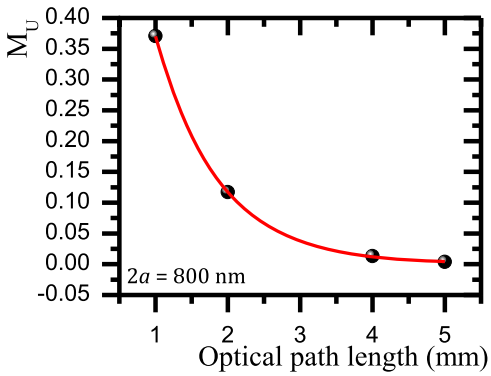

Figure 2. Beer–Lambert law for the collimated transmittance experiment of a suspension of polystyrene microspheres ($2a = 800$ nm). The red curve is an exponential fit.

Table 1. IAD results compared with Mie theory and collimated transmittance M_U (Beer–Lambert law).

	l^* (mm)	l_a (mm)	g
IAD	10.8120	75.2445	0.9116
Mie theory	11.9492		0.9166
M_U (fit)	11.2311		

4. Typical results from experiments

4.1. Fresnel coefficients and Beer–Lambert law

Usually, quick checks of the collimated transmittance experiment's proper operation are done previous to an experimental study: (a) measuring M_U, of deionized water in a cuvette (optical glass). Usually, a difference of around 0.33% is found from the theoretical value given by the Fresnel coefficients [55]. (b) The Beer–Lambert law on microsphere water suspensions (polystyrene, $2a = 800$ nm, $\phi = 0.000\,21$) can be evaluated using different optical path lengths. As expected, an exponential decay is measured with a coefficient of $1/\mu = 0.9799$ mm. Corrections due to the reflection of light on cuvette walls and water always have to be done. An example of these results is presented in figure 2.

Sample's optical parameters are recovered with the IAD method, and they were compared with theoretical results given by Mie scattering [45, 56]. Table 1 shows typical examples of obtained results. M_U (fit) comes from an exponential fit (figure 2), and the others from an IAD calculation for μ's, μ_a, and g. These results prove that our measurement methods are working reasonably well. Theory and experiments were in good agreement; deviation among them is 9.2% (Mie/IAD), and 6% (Mie/M_U (fit)).

4.2. MSD of microspheres when light absorption is present

As a test of the procedure described above, figure 3 presents results obtained with DWS for microsphere suspensions where Indian ink was added ($2a = 2$ μm, $\phi = 0.030$, $l^* = 150$ μm), to obtain a series of suspensions with different light absorption by adding successive aliquots, from a stock solution of ink (multiples 5 μl). At these dilutions, ink does not scatter light. Figure 3(a) shows the MSDs without any correction coming directly from the autocorrelation functions (equation (2)) presented in the inset of figure 3(a). As equation (3) predicted, the time delay in the autocorrelation functions shifts to longer times when the amount of ink increases. Artificially, at a particular time, MSDs are shorter as more ink is added to the suspension as if they had less diffusivity. As a consequence, longer times are needed to reach a specific MSD value. The intensity associated with longer paths is attenuated with absorption until they cannot be detected or correlated. The delay time in the autocorrelation function might be misinterpreted as a change in the probes' colloidal dynamics. The correction given by equation (4) is employed to overcome this issue, presented in figure 3(b). All the MSDs almost collapse on one curve, laying over the MSD of the original particle suspension without ink. A minor deviation to this rule is observed when 30 μl is added. This is probably because this suspension is slightly less concentrated than the nominal value due to ink addition, even though the agreement is satisfactory. A comparison with previous experiments can be made using figure 3(c). The MSDs and autocorrelation functions are shown for particles of $2a = 140$ nm ($l^* = 250$ μm), with different l_a values, without correction [36]. The shift on the autocorrelation function is also to longer times, which is more evident due to the particle diffusivity, which depends on the particle size. These are either the reasons that contribute to the difference between figures 3(a) and (c). Small particles diffuse more quickly than bigger ones, so they present longer MSDs. However, as absorption increases, MSDs of particles are shorter. The corrected MSD for the corresponding in figure 3(c) can be found in figure 3(d).

4.3. MSD of giant micelles without light absorption

Here we will present as examples two micellar systems with self-assembled WLMs, where light absorption is negligible. Figure 4 presents typical $\langle \Delta r^2(t) \rangle$ spanning over more than seven orders of magnitude in time curves obtained using 800 nm diameter microspheres dispersed in the micellar solutions. For CTAB/NaSal/water ($C_{CTAB} = 0.1$ M, R = [NaSal]/[CTAB] = 1, $T = 25$ °C) the $\langle \Delta r^2(t) \rangle$ is presented in figure 4(a), and for TDPS/SDS/brine ($C_{TDPS} = 0.046$ M, R = [SDS]/[TDPS] = 0.45, [NaCl] = 0.5 M, $T = 25$ °C) in figure 4(b). The $\langle \Delta r^2(t) \rangle$ curves are the result of a numerical inversion of equation (1), where the $g^{(1)}(t)$ came from DWS experiments shown in the insets. In these figures, we included the best-fit curves to the model curve proposed by Bellour *et al* (red lines) described above, where all the parameters D_o, D_m, δ^2, and γ' can be obtained. As observed in figure 4, the fittings are quite good.

4.4. MSD of giant micelles with light absorption

Certain diblock copolymers can form WLMs in water solutions, as is the case of 1, 4 poly(1, 3-butadiene)-polyethylene oxide (PBPEO) diblock copolymer; the degree of polymerization $m = 37$ for the PB block and $n = 45$ for the PEO block, $Mw = 4000$ g mol^{-1} (2000-*b*-2000) [28, 58]. Before adding probe particles to the WLM solutions made of PBPEO, the optical parameters were determined via the IAD method

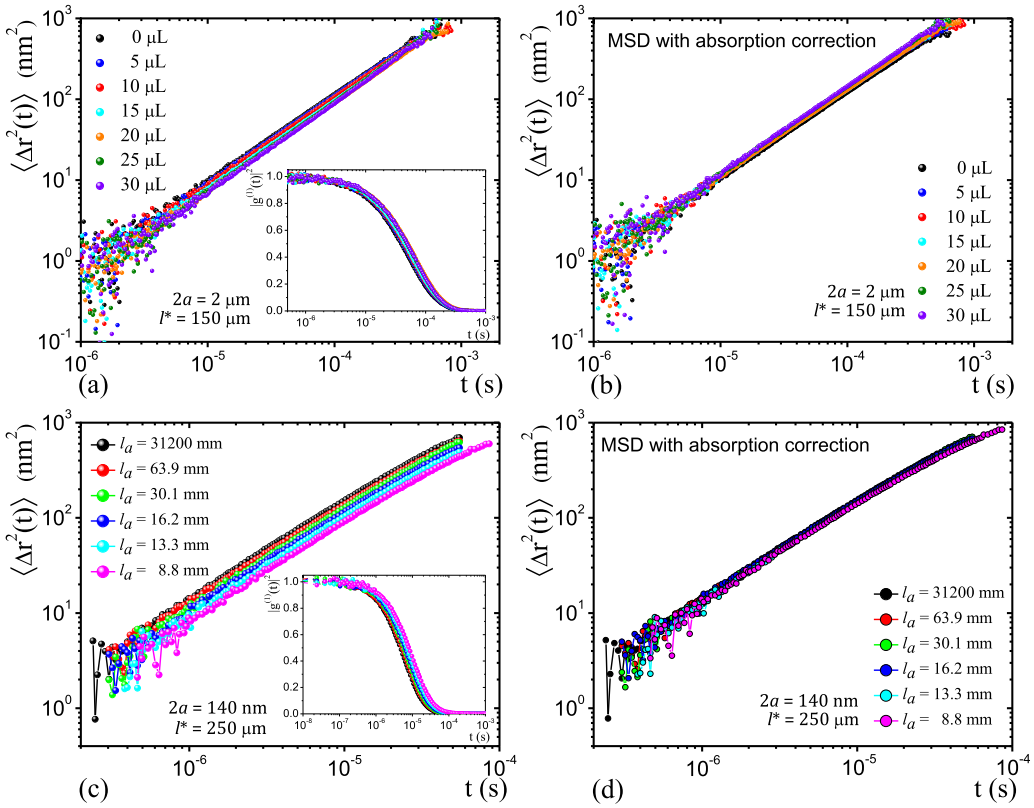

Figure 3. MSDs and correlation functions (a) MSDs for a suspension of microspheres of 2 μm, as a function of added ink without correction, obtained from correlation functions given in the inset. (b) MSDs of the suspensions presented in (a) corrected for absorption. All plots almost overlap on the curve for the case with no light absorption. (c) Comparison with a suspension with microspheres of 140 nm [36], where MSDs are presented as a function of l_a. Here, l_a was used instead of the amount of ink added. Inset: correlation functions for the different values of l_a. In both insets, the color code is the same as in the main figure. (d) Corrected MSD obtained from the correlation functions of (c), after ink addition, as a function of l_a. The extension to longer MSD times in some cases is notorious compared to the case with no absorption (black dots) [36].

because the PBPEO samples are opaque even at very low concentrations, see figure 5. As an example, at a concentration of 1.2 wt% of PBPEO, the recovered values are $l^* = 109.5$ mm, $l_a = 59.2$ mm, and $g = 0.8954$. They were obtained with a cuvette of an optical path length of 5 mm. According to these results, in this sample, light is significantly absorbed before it becomes random. However, it is possible to make DWS experiments with a small contribution of scattered light.

As a test for our procedure to treat light absorption, we artificially increased even more the micellar solution's absorption by adding Indian ink in the same way described above. A series of suspensions with different light absorption levels was prepared by adding successive aliquots from a stock ink solution (multiples 5 μl). Figures 6 and 7 present the results for two micellar solutions (1.5 wt% and 2 wt%) with suspended microspheres of $2a = 2$ μm at $\phi = 0.030$.

The correction for absorption is significant in all cases. The results are quite satisfactory because they lay over a single curve after employing the correction. An exception occurs at longer times, where a deviation from the expected value shows up for all the cases. This is due to a lack of data at long correlation times. 900 s of data collection is not sufficient to obtain good quality data at these stages; however, in this particular case, the system's nature does not permit measurements for longer times: probe particles precipitate easily due to their size and the low PBPEO solution viscosity (<1 Pa s). It is often possible to observe a feature in the corrected MSD vs t curves; they can reach longer times when ink is added, independently from the lack of data at longer times in the case of PBPEO suspensions. As the correlation function is moved to longer times due to the contribution of l_a values in the factor l^*/l_a on the equation (3), the tail of $g^{(1)}(t)$ goes not so fast to zero, permitting to extend the MSDs numerical calculations. This effect can be observed in 140 nm microspheres in figure 3(d) from data in reference [36]; this extension effect is apparent once the correction for absorption is done. The degree of extension is still a question to answer, and further experiments should be performed.

Figures 8(a) and (b) present a plot of l^* vs l_a for four PBPEO concentrations to determine where our measurements are valid within the diffusion approximation. l^* values are essentially constant. The same sample was used for each ink addition, so particle fill fractions were not recalculated because the change was very small. The figure's dashed line corresponds to $l^* = 150$ μm, which is a prediction from Mie's theory for the scattering coefficient [45] computed for that particle size and volume fraction estimates for polystyrene particles in water. This value varies from experimental ones, possibly due to

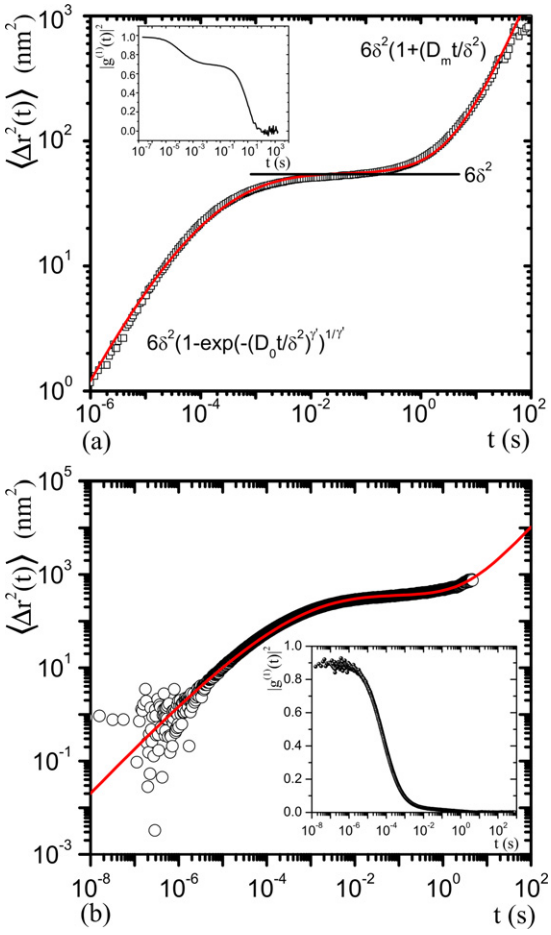

Figure 4. A typical $\langle \Delta r^2(t) \rangle$ curve obtained in a DWS experiment in WLM solutions using microspheres of a diameter of 800 nm of the systems (a) CTAB/NaSal/water, parameters of the fitting curve: $6\delta^2 = 49.9$ nm^2, $D_m = 20.11 \times 10^{-17}$ m^2 s^{-1}, and $\gamma' = 0.26$. Reprinted with permission by Springer Nature Customer Service Centre GmbH: [Springer Nature] [The European Physical Journal] [30]. (b) TDPS/SDS/brine, parameters of the fitting curve: $6\delta^2 = 351$ nm^2, $D_m = 1.67 \times 10^{-17}$ m^2 s^{-1}, and $\gamma' = 0.274$. Reprinted with permission from [57]. Copyright 2010 American Chemical Society. Insets correspond to the intensity time correlation function for the same solution. We included the best-fit curves to the model curve proposed by Bellour *et al* [51] (red lines).

particles' sedimentation, which is relatively fast in samples with low viscosity, as mentioned before. Error bars represent the maximum and minimum l^* measured values before and after DWS experiments that are attributed to particle sedimentation. Figure 8(c) shows a plot of L/l^* vs l_a/l^*. The cross-hatched region in this plot is the allowed one where the diffusion approximation of light is valid, i.e., $9 \leqslant L/l^* \leqslant 25$ and $l_a/l^* \geqslant 30$. In all cases, the diffusion approximation is achieved.

4.5. From the MSD to the viscoelastic moduli

As mentioned above, there are different procedures to determine the viscoelastic modulus. Here, we discuss three of them to give a clear idea of the results they produce. In the first one, equation (6) is used with the logarithmic derivative, equation (7). In the second one, $J(t)$ is evaluated through equation (8), and $G^*(\omega)$ is computed using equation (9). In the third method, the unilateral Fourier transform is performed

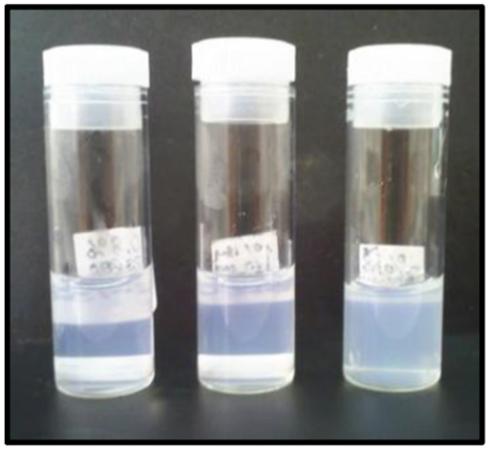

Figure 5. PBPEO WLM samples at concentrations of 1.2 wt% are not transparent.

on the best fits of the Bellour *et al* model described above to the $\langle \Delta r^2(t) \rangle$ experimental curves, as indicated in equation (6). Figure 9 presents the moduli obtained for two different WLM solutions using the three mentioned procedures applied to the typical experimental MSD presented in figure 4. The results of mechanical rheology were included for comparison. All methods, most of the time, follow the same trend. However, the two first methods are pretty noisy, particularly after the crossing. This is not the case when the Bellour *et al* model is used. Noise is quite damaging either around the minimum in $G''(\omega)$ because it determines the value of l_e/L_C, and at high frequencies where the frequency ω_o is obtained through a slope change in $|G^*(\omega)|$ that allows us to estimate l_p. The origin of that noise is apparently because the $\langle \Delta r^2(t) \rangle$ experimental curves are not analog functions; they are couples of series of numbers $(\langle \Delta r^2(t) \rangle, t_i)$, coming from the correlation functions given by a digital correlator through equation (2). Using the Bellour *et al* method from the beginning produces an analogic function, which avoids noise propagation and correctly extends the MSD data close to short and long times, where the correlation function could be noisy. We conclude that for estimating the characteristic lengths of the WLM network, the use of the best fits of the Bellour *et al* model to the experimental data is more reliable.

4.6. Viscoelastic spectra for giant cylindrical micelles without light absorption

The viscoelastic spectra for the WLM solutions that we will describe here were obtained applying a Laplace transform using $z \to i\omega$ (analytic continuity) in equation (6) to obtain the real and complex components of $G^*(\omega)$, where $\langle \Delta r^2(t) \rangle$, as explained above, was obtained by best fitting a model curve to the experimental values of $\langle \Delta r^2(t) \rangle$ vs t. Examples of results for two different systems (CTAB/NaSal/water and TDPS/SDS/brine) are shown in figure 10, where the elastic and viscous moduli are presented as a function of the frequency [30, 57]. The same kind of data is also presented, at low and intermediate frequencies, determined with a mechanical rheometer. The agreement between the moduli

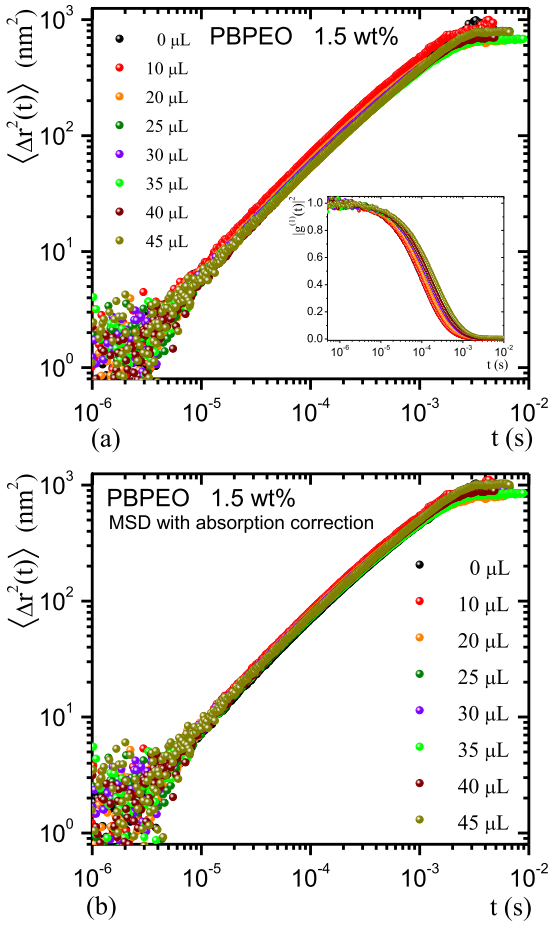

Figure 6. Results for WLM solutions made of PBPEO at 1.5 wt% as a function of added ink. (a) MSD for the correlation functions given in the inset, when no correction for absorption is used. (b) MSD for the examples presented in (a), including the correction for absorption.

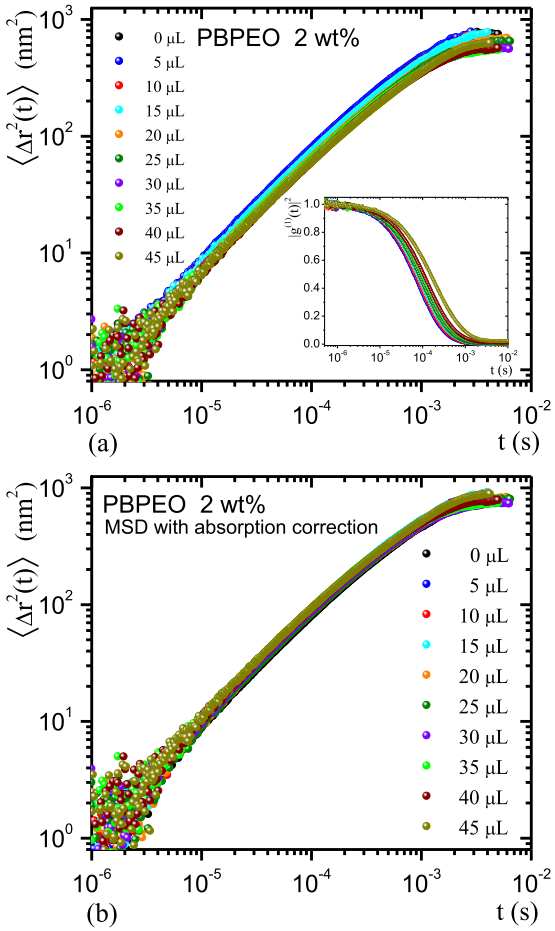

Figure 7. Results for solutions made of PBPEO at 2 wt% as a function of added ink. (a) MSD for the correlation functions given in the inset, when no correction for absorption is used. (b) MSD for the examples presented in (a), including the correction for absorption.

obtained by mechanical rheometry and DWS is quite well, at low and intermediate frequencies, where the behavior of the fluids is Maxwellian (a Cole–Cole plot can show this easily) [30, 59]. Here, stress relaxation occurs mainly through micellar reptation and micellar breaking and recombination; as a consequence, a single relaxation time dominates. The plateau modulus and the relaxation time are obtained from the first crossover. DWS micro-rheology reaches a bandwidth far beyond the conventional rheometry, allowing us to observe two crossovers in $G^*(\omega)$. Probe size and solvent inertial effects are negligible below frequencies of $\omega = 10^6$ rad s^{-1}. At time scales shorter than those of WLM breakage time, which occurs at high frequencies, the Maxwellian stress relaxation processes are essentially frozen, and micelles can be considered as semiflexible chains. Stress relaxes through intramicellar processes: first, it is dominated by the Rouse–Zimm modes and then by the internal relaxation of individual Kuhn segments. In this frequency range, G^* exhibits a power-law behavior, $G^* \sim \omega^{\nu}$, with the exponent $\nu \sim 5/9$ in the Rouse–Zimm regime which switches to $\nu \sim 3/4$, where internal bending modes of Kuhn segments dominate. This change occurs at a frequency ω_o corresponding to the shortest relaxation time in the Rouse–Zimm spectrum. This feature can be observed in the inset of figure 10(b). Another important feature to be pointed out is related to the local minimum of $G''(\omega)$ after the first crossing between $G'(\omega)$ and $G''(\omega)$ denoted by $G''_{\min}$. This is usually better defined in DWS micro-rheology than in mechanical rheometry and will be important for estimating the characteristic lengths of the WLMs in the solution, as shown below.

4.7. Viscoelastic spectra for giant cylindrical micelles with light absorption

We previously discussed the absorption in PBPEO WLMs; the resulting $G'(\omega)$ and $G''(\omega)$ coming from MSDs are described in reference [58]. Now, we will discuss a different class of systems. Several WLM solutions have been reported with the ability to respond to external stimuli when specific molecules are incorporated within the micelles. These stimuli can be a temperature change, light irradiation, pH variations, etc, and they can generate a structural change in the system. For example, azobenzene derivatives are photoswitchable molecules presenting a trans-cis isomerization when they are UV-irradiated. When incorporated into the micelles, UV irradiation can break them, and the rheological properties can be drastically modified in some cases. These systems, called smart materials,

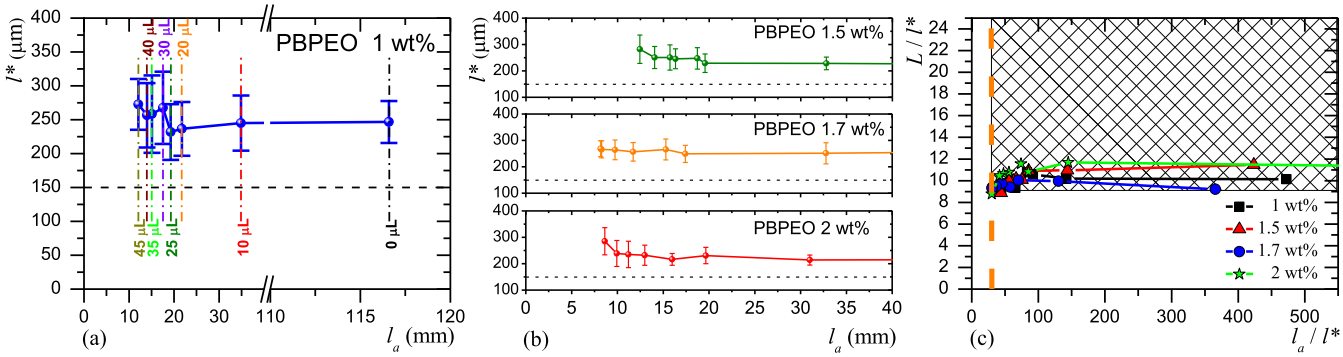

Figure 8. Variation of l^* vs l_a for four micellar solutions of PBPEO. (a) 1 wt%. It also indicates the quantities of ink added with the same code of colors as in previous figures. (b) 1.5 wt%, 1.7 wt%, and 2 wt%. Horizontal dashed lines refer to Mie's theory predicted value of $l^* = 150$ μm. Error bars include the maximum and minimum of each measured value of l^*. (c) Variation of L/l^* vs l_a/l^*. The cross-hatched area is where L/l^* and l_a/l^* are valid in the diffusion approximation. The vertical dashed line is placed at $l_a/l^* = 30$.

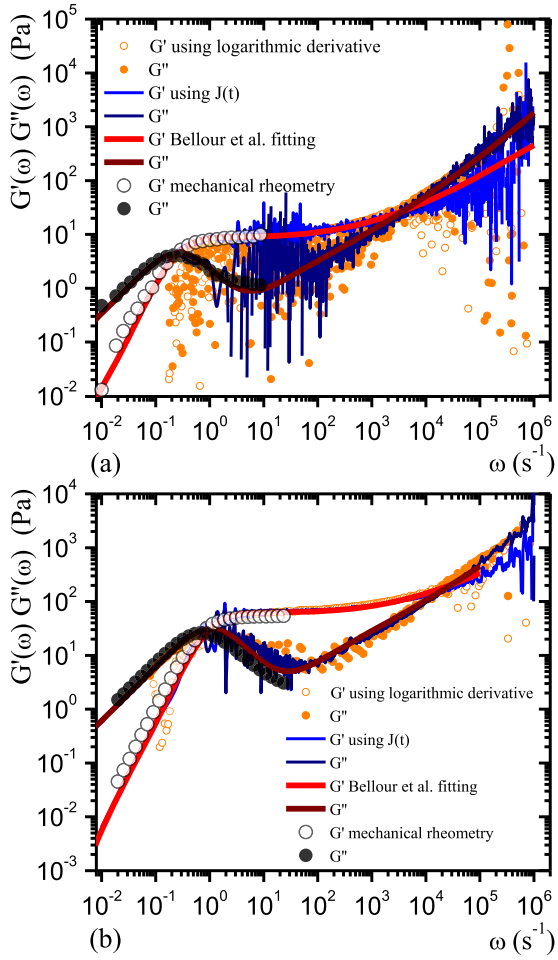

Figure 9. Typical $G'(\omega)$ and $G''(\omega)$ obtained for two WLM solutions (a) CTAB/NaSal/water ($C_{CTAB} = 0.1$ M, $R = 2$, at 22 °C) and (b) TDPS/SDS/brine ($C_{TDPS} = 0.046$ M, $R = 0.45$, $C_{NaCl} = 0.5$ M, $T = 25$ °C) using microspheres of a diameter of 800 nm. They were obtained from the MSD of figure 4 with three procedures: equation (6) in conjunction with the logarithmic derivative; $J(t)$ evaluated through equation (8), and $G^*(\omega)$ evaluated using equation (9); the unilateral Fourier transform is performed on the best fits to the Bellour *et al* model to the $\langle \Delta r^2(t) \rangle$ experimental curves, through equation (6). Moduli obtained from mechanical rheometric measurements were included for comparison.

can be used in different material science applications and are of much interest [60]. Here, we will present WLM solutions where a small chromophore, 4-(phenylazo)benzoate ion ($AzoCOO^-$) is added [61, 62]. The main challenge to get information with DWS in these micellar solutions is the high light absorption of azo compounds. UV–Vis experiments reveal a significant absorption contribution in these compounds around 514 nm, which is in the range of the laser's wavelength used in DWS experiments. A measurement employing the IAD method for a sample of only $AzoCOO^-$ at 20 mM concentration without colloidal microspheres gives an idea of the aromatic molecules' absorption strength. The optical path length was varied with cuvettes of different widths. Scattering events were negligible, but $l_a = 2.33$ mm remained on the average. Figure 11 presents M_U vs the optical path length, showing an exponential decay that agrees with the Beer–Lambert law; $1/\mu = 2.3 \pm 0.1$ mm.

Following the procedures described above, to prepare DWS experiments, table 2 summarizes the optical parameters obtained from the micellar solutions of CTAB/NaSal/$AzoCOO^-$ when probe functionalized microspheres were added ($2a = 800$ nm, amine-functionalized, $\phi = 0.035$). However, at higher $AzoCOO^-$ concentration, it was impossible to perform collimated transmittance measurements because of the large amount of absorbed light due to the chromophore. We also added NaCl to the WLM solution, TDPS/SDS/NaCl/$AzoCOO^-$, which would increase the micellar total contour length. The results are similar to those of CTAB/NaSal/$AzoCOO^-$ (see table 3). In both micellar solutions, the values of L/l^* provide sufficiently l^* steps for light beams to assure multiscattering events. Although for many solutions $l_a/l^* \geqslant 30$, these values were not sufficiently high as recommended in a few cases. It was possible to measure the correlation functions assuring the diffusion regime of light. We will comment on it later.

Figure 12(a) shows $g^{(1)}(t)$ vs t curves for microemulsions of CTAB/NaSal/$AzoCOO^-$ at different $AzoCOO^-$ concentrations, and the inset presents the same sort of curves for the TDPS/SDS/NaCl/$AzoCOO^-$. Figure 12(b)

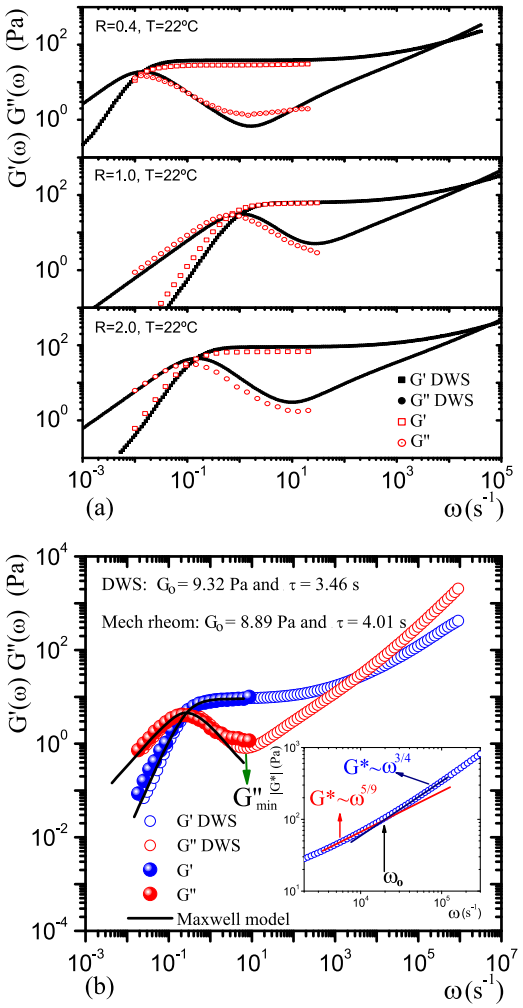

Figure 10. Viscoelastic spectra of the same solutions from figure 4 for (a) CTAB/NaSal/water for different R values and at the same temperature. Reprinted with permission by Springer Nature Customer Service Centre GmbH: Springer Nature. The European Physical Journal. [30]. Red colored symbols correspond to data obtained using mechanical rheometry. (b) TDPS/SDS/brine shows the key points to determine the characteristic lengths of the WLM network. Reprinted with permission from [57]. Copyright 2010 American Chemical Society. Full circles are the data from mechanical rheometry (blue $G'(\omega)$, red $G''(\omega)$), and lines represent the best fit to a Maxwell fluid model. The inset shows $G^* \sim \omega^{\nu}$ at high frequencies; here, ν in the power-law changes from 5/9 to 3/4.

Table 2. Optical parameters calculated using the IAD method. The values correspond to all different CTAB/NaSal/AzoCOO$^-$ samples studied.

AzoCOO$^-$	0	5 mM	10 Mm	15 mM
l_a (mm)	31.070	5.7700	2.8100	2.5200
L/l^*	14.780	17.250	13.250	13.180
l_a/l^*	404.04	39.780	14.890	13.260

shows the MSDs vs t curves corrected for absorption of CTAB/NaSal/AzoCOO$^-$ and in the inset, the case of TDPS/SDS/NaCl/AzoCOO$^-$. In both micellar solutions, $g^{(1)}(t)$ curves are surely shifted to longer times due to light

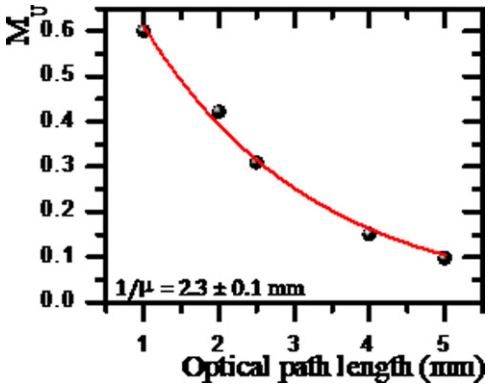

Figure 11. Collimated transmittance measurements in a solution of AzoCOO$^-$ (20 mM) without added microspheres. Various cuvettes with different optical path lengths were used in these experiments. The red curve is an exponential fit. The fit confirms that the decaying effect is just due to light absorption. The AzoCOO$^-$ does not scatter visible light.

Table 3. Optical parameters calculated using the IAD method. The values correspond to all different TDPS/SDS/NaCl/AzoCOO$^-$ samples studied.

AzoCOO$^-$	0	5 mM	10 mM
l_a (mm)	159.95	5.2200	2.6600
L/l^*	16.270	19.720	14.830
l_a/l^*	1041.3	41.180	15.750

absorption as the AzoCOO$^-$ concentration increases. However, the addition of chromophore also modifies the micellar structure, which is the ultimate information pursued by the experimentalist interested in the solutions' physicochemical properties, not in light absorption. $g^{(1)}(t)$ curves look different as the AzoCOO$^-$ concentration increases due to the system's mentioned structural changes. The changes are more evident in the corrected MSDs vs t plots. When AzoCOO$^-$ is not added, the autocorrelation functions present two-time decays; the second one appears to be quite delayed with respect to the first decay. In contrast, when the chromophore is added, the time decays are not so separated. This feature can be interpreted as a sign of different relaxation time scales due to tubular structures with different length scales in the micellar solution. As it can be observed in these figures, as the AzoCOO$^-$ concentration increases, it was possible to obtain an intensity correlation function, despite the fact that $l_a/l^* \geqslant 30$ is not strictly obeyed. However, at short times, these functions present noise, which is translated to the MSDs.

Figure 13 presents the viscoelastic spectra for the micellar solutions of CTAB/NaSal, and in figure 14 for TDPS/SDS/NaCl; in both cases, varying concentrations of AzoCOO$^-$. We included the moduli obtained with microrheology covering a broad range of frequencies (more than seven orders of magnitude). For comparison, we also included the moduli at low and medium frequencies obtained by mechanical rheology. The black lines are fittings of the Maxwell model at low and intermediate frequencies. The crossing points provide the G_o values and relaxation times.

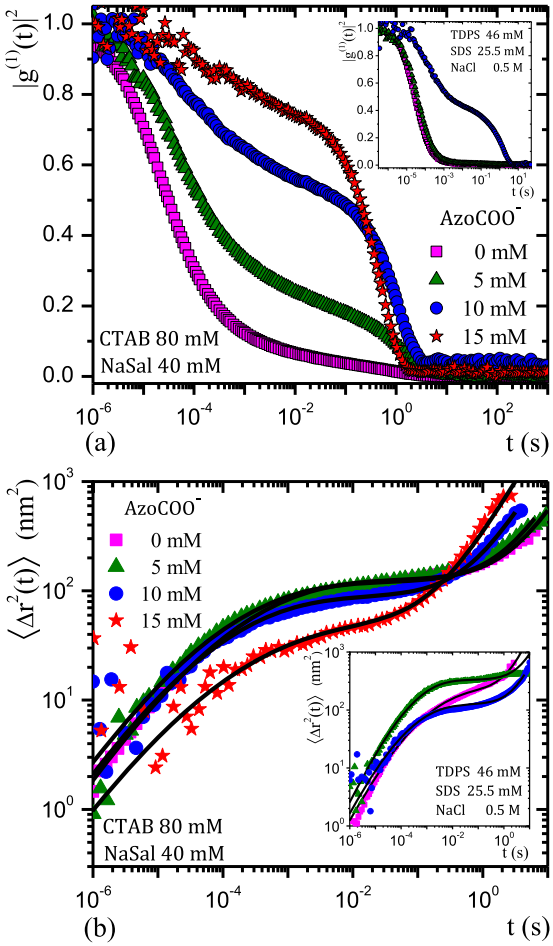

Figure 12. Results in two micellar systems: (a) $g^{(1)}(t)$ vs t for the micellar solutions of CTAB/NaSal where AzoCOO$^-$ was added. Inset: $g^{(1)}(t)$ curves for micellar solutions of TDPS/SDS/NaCl/AzoCOO$^-$. (b) The corresponding MSD vs t plots for (a). Inset: the same plots for TDPS/SDS/NaCl/AzoCOO$^-$ microemulsions for the correlation functions in the inset of (b). The color code is the same as in the main figure. Black lines correspond to the Bellour *et al* model fittings. Reprinted with permission from [61]. Copyright 2019 American Chemical Society. Reprinted from [62], Copyright 2021, with permission from Elsevier.

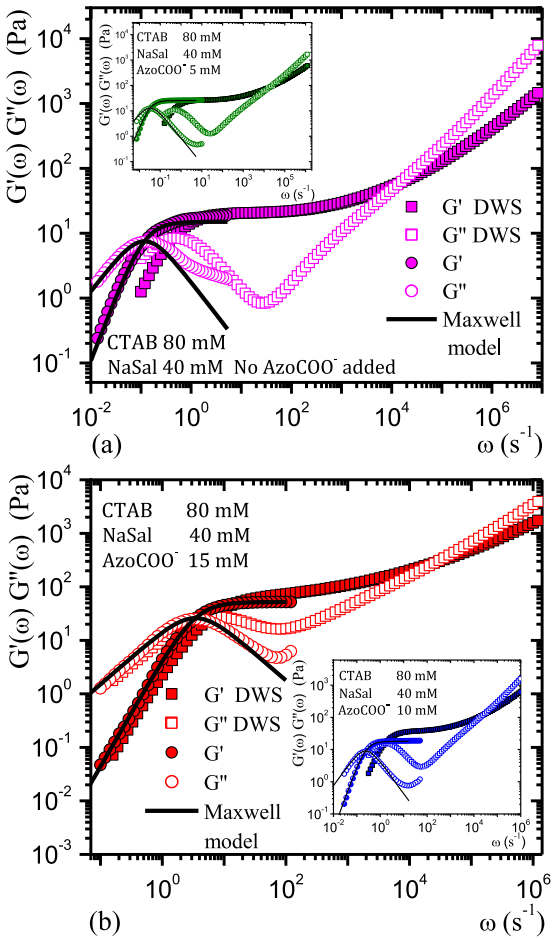

Figure 13. Viscoelastic spectra of micellar solutions of CTAB/NaSal with different concentrations of AzoCOO$^-$ obtained by micro-rheology (squares) where we used MSDs corrected for light absorption (main and corresponding inset plots). For comparison, results of mechanical rheology are included (circles). Black lines are fittings to the Maxwell model for the mechanical rheology. Full symbols are the storage moduli, and open symbols are the loss moduli, independently of the plot color. Reprinted with permission from [61]. Copyright 2019 American Chemical Society.

The viscoelastic spectra coming from DWS and mechanical rheology are quite similar for the micellar solutions. However, sometimes, the former ones are displaced to higher frequencies with respect to the latter ones. This is evident at the crossing between $G'(\omega)$ and $G''(\omega)$. Nevertheless, G_o values obtained from both kinds of measurements are almost the same. The major difference occurs in the relaxation times. In those cases, the measured relaxation times with DWS give shorter values due to the frequency displacement. These features cannot be attributable to light absorption corrections because they are observed in some DWS experiments of transparent fluids, as in the examples without chromophore given in figures 13(a) and 14. In previous experiments, it has been pointed out that for relaxation times < 10 s, the deviation between both methods is more significant ($\sim$ one order of magnitude) [57]. It was suggested that hydrotrope salt ions in the solution could be responsible for this deviation [63]. Here, the chromophore is playing this role. However, this suggestion is not supported by experimental work. Quite recently [49], possible problems of numerical nature using analytical continuation have been reported, going from the Laplace transform of the relaxation modulus to the frequency domain dynamic moduli. However, as we analyzed above, it seems not to be the case. Nevertheless, we can not discard that residual effects of the MSD fitting could produce small deviations in $G'(\omega)$ and $G''(\omega)$ obtained by our procedure. Curiously in figure 13(b), for the CTAB and NaSal at 15 mM AzoCOO$^-$, DWS and mechanical spectra are very close. The more substantial discrepancy occurs when AzoCOO$^-$ is concentrated at 5 mM (inset figure 13(a)) and 10 mM (inset of figure 13(b)). In the case of the micellar solutions of TDPS/SDS/NaCl/AzoCOO$^-$, the same features were observed (figure 14). Finally, it has been suggested that the real and imaginary parts of $G^*(\omega)$, which are determined in a mechanical oscillatory shear experiment from the amplitude and phase shift of the response signal, are much

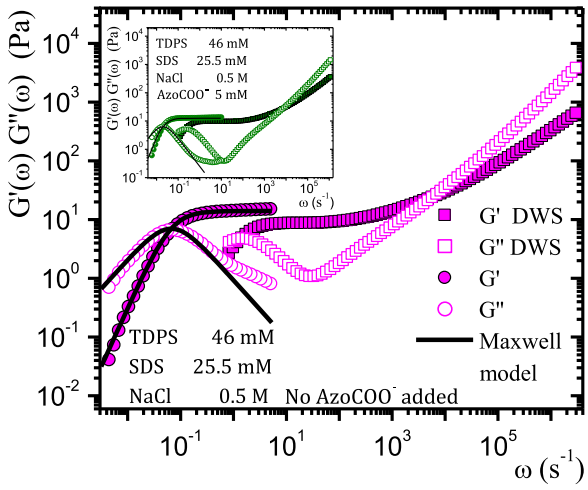

Figure 14. Viscoelastic spectra for microemulsions of TDPS/SDS/NaCl with different concentrations of AzoCOO$^-$, obtained by micro-rheology (squares). Here we used MSDs corrected for light absorption (main and corresponding inset plots). For comparison, results of mechanical rheology are included (circles). Black lines are fittings to the Maxwell model for the mechanical rheology. Full symbols are the storage moduli, and open symbols are the loss moduli, independently of the plot color. Reprinted from [62], Copyright 2021, with permission from Elsevier.

more accurate than those of DWS, where the MSD is measured in time-space.

5. Typical mesoscopic scales in giant cylindrical micelles

As mentioned in the introduction, at high frequencies, $G^*(\omega)$ exhibits a power-law behavior, $|G^*| \sim \omega^{\nu}$, where an exponent change occurs at ω_o due to a change in the dominant modes of relaxation. From ω_o, which is observed as a slope change in $|G^*(\omega)|$, l_p can be obtained, and with this data, all other length scales of the network formed by the WLMs can be computed, namely, L_C, l_e, and ξ. In micellar solutions that absorb light, we can access this information because we are able to obtain the complex modulus at high frequencies implementing the absorption correction.

The ability to reach high frequencies makes micro-rheology a complementary alternative to standard static scattering techniques to obtain structural information of cylindrical micelles embedded in a fluid. DWS results allow us to have $G^*(\omega)$ at high frequencies. These quantities change when the amount of surfactant, the ratio of hydrotrope salt to surfactant, temperature, or ionic strength of the media vary. It is essential to mention that theory developed for WLMs is far from being complete. Over the last decade, several small but significant changes have been made to the original formulas developed to estimate these characteristic lengths [11, 25–27].

In figure 15(a), data obtained from [30], show how the characteristic lengths vary for the system CTAB/NaSal as we vary the R = [NaSal]/[CTAB] as well as the temperature. The characteristic lengths were corrected to take into account the improvements in the way to calculate them using the formulas given in the introduction [11, 25–27]. As we can observe, l_p, l_e, and ξ are quite insensible to variations of R and temperature. On the contrary, L_C is quite sensible; these WLMs are extremely large, and their contour length can vary more than one order of magnitude varying R. Although the temperature is varied in a very short range, it is pretty evident that as temperature increases, L_C decreases. The ratio of L_C/l_e also decreases with the temperature, explaining why the lower temperature corresponds to a larger viscosity. Entanglement decreases on increasing temperature, which also explains why in this micellar solution, the elasticity number (ratio of Wi number, $Wi = \dot{\gamma}\tau$ over the Reynolds number) measured in Couette flow decreases when increasing temperature. The upper panel of figure 15(b) presents L_C as a function of the azo compound, which was added to be incorporated into the WLMs of the mentioned systems: TDPS/SDS/NaCl [62] and CTAB/NaSal/NaCl [61]. L_C decreases exponentially with the increase of AzoCOO$^-$ concentration in CTAB/NaSal/NaCl. However, in TDPS/SDS/NaCl, L_C increases to a maximum at [AzoCOO$^-$] $\sim$ 5 mM. For 10 mM, L_C reaches the same value as the original micellar solution without chromophore. The lower panel of figure 15(b) presents l_e, l_p, and mesh size ξ as a function of the azo concentration for the micellar solution TDPS/SDS/NaCl. l_p and ξ almost do not significantly change with the increment of the AzoCOO$^-$ concentration, but l_e decreases. The ratio L_C/l_e increases in samples when the chromophore is added, compared to the micellar solution without chromophore; for [AzoCOO$^-$] = 0, 5, and 10 mM; L_C/l_e = 14.4, 62.5, and 20.3, respectively. There is more entanglement per average micelle, which could be one of the reasons to have an increase in viscosity at low $\dot{\gamma}$ in the samples increasing the AzoCOO$^-$ concentration [62]. A larger entanglement hampers flow in micellar solutions with added chromophore in comparison with the micellar solutions without chromophore. Figure 15(c) shows how L_C increases as the ionic strength in the solution increases by adding NaCl, as described in [57]. As the ionic strength of the media increases, the micelles are discharged, and there is an increase in their scission energy, which promotes a linear growth of the WLMs. Although, after a maximum, there is a decrease in L_C. Also, in this system, L_C is shorter as the temperature increases for the same quantity of added salt, and L_C also grows with the increase of the zwitterionic surfactant concentration, C_z, following a power-law $L_C \sim C_z^{\beta}$ [57]. Surprisingly, there is no significant variation of l_p, l_e, and ξ with salt concentration and temperature changes; only l_e presents a slight decrease as the temperature increases. WLMs of diblock copolymers have also been studied with the procedure described here. In the system made of WLMs of a PB-PEO [58], l_p has been obtained, and it was shown that the interaction between WLMs sensibly modifies l_p, since it increases as the concentration decreases close to C^*, giving values close to those of SANS measurements (0.5 wt% $\sim l_p$ = 225 nm). The explanation of this behavior was given in reference [58].

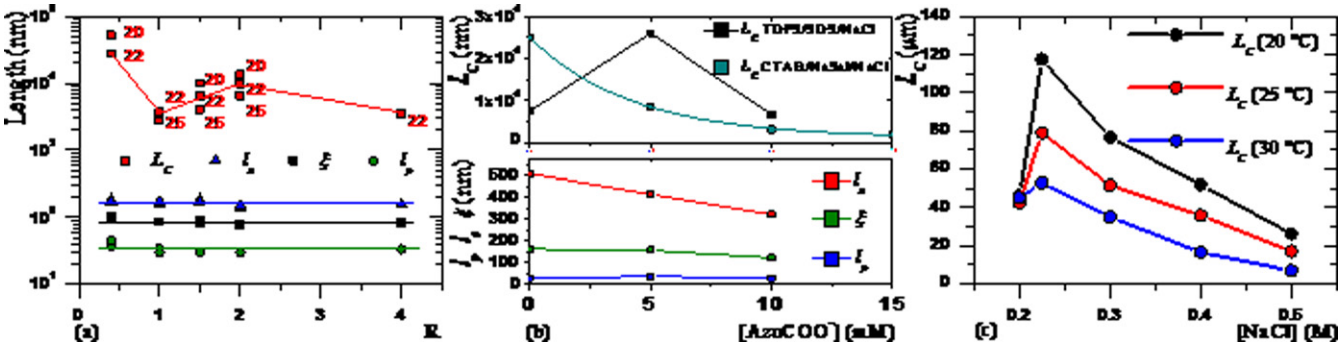

Figure 15. Characteristic lengths in WLM solutions. Lengths were recalculated from the original reports to take into account the changes in the formulas for calculating them, as given in the introduction. (a) CTAB/NaSal: R = [NaSal]/[CTAB], [CTAB] = 0.1 M from [30]. Numbers to the right of the symbols indicate temperature in °C. (b) Upper panel: L_C vs [AzoCOO$^-$] for two systems at 25 °C and pH = 12: TDPS/SDS/NaCl (R = [SDS]/[TDPS] = 0.55, [TDPS] = 46 mM) and CTAB/NaSal/NaCl (R = [NaSal]/[CTAB] = 0.5, [CTAB] = 80 mM) in both cases as a function of the added azo compound [61, 62]. Lower panel: l_e, l_p and ξ vs [AzoCOO$^-$] for TDPS/SDS/NaCl (R = [SDS]/[TDPS] = 0.55, [TDPS] = 46 mM) [62]. (c) L_C as function of brine concentration at different temperatures for TDPS/SDS/NaCl (R = [SDS]/[TDPS] = 0.55, [TDPS] = 46 mM). In all figures, lines are guides to the eye.

6. Conclusions

The whole procedure for determining the mesoscopic scales in micellar solutions embedded with giant cylindrical micelles was presented performing quasi-elastic multiple light scattering experiments. In particular, we discussed how the scattering experiments were conducted with DWS, how to solve the problems of recovering the optical parameters from micellar solutions implementing the IAD method, which are indispensable in developing measurements with this spectroscopy, and how to treat the absorption in the case micellar solutions also absorb light. The capacity for reaching $G^*(\omega)$ at high frequencies makes micro-rheology complementary to standard scattering techniques for obtaining structural information in a fluid with embedded cylindrical micelles. $G^*(\omega)$ allows us to estimate the important characteristic lengths of the WLM network as L_C, l_p, l_e, and ξ, which determine the dynamical behavior in these systems employing approximate relations coming from WLM theory. These mesoscopic characteristic lengths depend on the solution's physicochemical parameters, and we showed that these lengths could be helpful to understand the rheological behavior of WLM solutions. This is an available tool for getting a different perspective of what is occurring in solutions made of giant micelles providing a helpful physical insight not available with other techniques.

Acknowledgments

We acknowledge the financial support of SEP-CONACyT (Project: A1-S-15587) and DGAPA-UNAM (IN 106321). Special thanks to Dr Erick Sarmiento-Gómez for his helpful discussions and ideas.

Data availability statement

All data that support the findings of this study are included within the article (and any supplementary files).

ORCID iDs

Antonio Tavera-Vázquez https://orcid.org/0000-0001-8304-2123
Natalia Rincón-Londoño https://orcid.org/0000-0002-8722-7982
Rolando Castillo https://orcid.org/0000-0001-6331-0311

References

[1] Boyd R H and Smith G D 2007 *Polymer Dynamics and Relaxation* (Cambridge: Cambridge University Press)
[2] Macosko C W 1994 *Rheology: Principles, Measurements and Applications* (New York: Wiley)
[3] Furst E M and Squires T M 2017 *Microrheology* (Oxford: Oxford University Press)
[4] Gardel M L, Valentine M T and Weitz D A 2005 *Microrheology—Microscale Diagnostic Techniques* ed ed K S Breuer (Berlin: Springer)
[5] Waigh T A 2016 *Rep. Prog. Phys.* **79** 074601
[6] López-Díaz D and Castillo R 2011 *Soft Matter* **7** 5926
[7] Boskovic S, Chon J W M, Mulvaney P and Sader J E 2002 *J. Rheol.* **46** 891
[8] Darwiche A, Ingremeau F, Amarouchene Y, Maali A, Dufour I and Kellay H 2013 *Phys. Rev.* E **87** 062601
[9] Dufour I *et al* 2011 *J. Sensors* **2012** 719898
[10] Zakharov P, Cardinaux F and Scheffold F 2005 *Phys. Rev.* E **73** 011413
[11] Willenbacher N, Oelschlaeger C, Schopferer M, Fischer P, Cardinaux F and Scheffold F 2007 *Phys. Rev. Lett.* **99** 068302
[12] Mason T G and Weitz D A 1995 *Phys. Rev. Lett.* **74** 1250
[13] Mason T G, Gang H and Weitz D A 1997 *J. Opt. Soc. Am.* A **14** 139
[14] Mason T G 2000 *Rheol. Acta* **39** 371
[15] Linder P and Zemb T (ed) 2002 *Neutrons, X-Ray and Light Scattering Methods Applied to Soft Condensed Matter* (Amsterdam: North-Holland)
[16] Seto H, Kato T, Monkenbusch M, Takeda T, Kawabata Y, Nagao M, Okuhara D, Imai M and Komura S 1999 *J. Phys. Chem. Solids* **60** 1371
[17] Nettesheim F and Wagner N J 2007 *Langmuir* **23** 5267
[18] Shikata T, Dahman S J and Pearson D S 1994 *Langmuir* **10** 3470

[19] von Berlepsch H, Harnau L and Reineker P 1998 *J. Phys. Chem.* B **102** 7518
[20] Acharya D P and Kunieda H 2006 *Adv. Colloid Interface Sci.* **123–126** 401
[21] Ezrahi S, Tuval E and Aserin A 2006 *Adv. Colloid Interface Sci.* **128–130** 77
[22] Dreiss C A 2007 *Soft Matter* **3** 956
[23] Yang J 2002 *Curr. Opin. Colloid Interface Sci.* **7** 276
[24] Cates M E 1987 *Macromolecules* **20** 2289
[25] Zou W and Larson R G 2014 *J. Rheol.* **58** 681
[26] Granek R and Cates M E 1992 *J. Chem. Phys.* **96** 4758
[27] Granek R 1994 *Langmuir* **10** 1627
[28] Arenas-Gómez B, Vinceković M, Garza C and Castillo R 2014 *Eur. Phys. J.* E **37** 51
[29] Berret J F, Appell J and Porte G 1993 *Langmuir* **9** 2851
[30] Galvan-Miyoshi J, Delgado J and Castillo R 2008 *Eur. Phys. J.* E **26** 369
[31] Turner M S and Cates M E 1991 *Langmuir.* **7** 1590
[32] Pine D J, Weitz D A, Zhu J X and Herbolzheimer E 1990 *J. Phys. France* **51** 2101
[33] Weitz D A and Pine D J 1993 *Diffusing-Wave Spectroscopy in Dynamic Light Scattering: The Method and Some Applications* ed ed W Brown (Oxford: Oxford University Press)
[34] van Zanten J H and Rufener K P 2000 *Phys. Rev.* E **62** 5389
[35] Cardinaux F, Cipelletti L, Scheffold F and Schurtenberger P 2002 *Europhys. Lett.* **57** 738
[36] Sarmiento-Gómez E, Morales-Cruzado B and Castillo R 2014 *Appl. Opt.* **53** 4675
[37] Prahl S A, van Gemert M J C and Welch A J 1993 *Appl. Opt.* **32** 559
[38] Prahl S A 2017 Inverse adding doubling http://omlc.ogi.edu/software/iad/index.html
[39] Prahl S A 2011 https://omlc.org/software/iad/manual.pdf
[40] Hajjarian Z and Nadkarni S K 2014 *Opt. Express* **22** 6349
[41] Zhang C, Reufer M, Gaudino D and Scheffold F 2017 *Korea Aust. Rheol. J.* **29** 241
[42] Carslaw H S and Jaeger J C 1990 *Conduction of Heat in Solids* (Oxford: Clarendon)
[43] Scheffold F 2002 *J. Dispersion Sci. Technol.* **23** 591
[44] Durduran T, Yodh A G, Chance B and Boas D A 1997 *J. Opt. Soc. Am.* A **14** 3358
[45] Ishimaru A 1978 *Wave Propagation and Scattering in Random Media: Single Scattering and Transport Theory* vol 1 (New York: Academic)
[46] Wang L V and Wu H 2007 *Biomedical Optics: Principles and Imaging* (New York: Wiley)
[47] Kaplan P D, Kao M H, Yodh A G and Pine D J 1993 *Appl. Opt.* **32** 3828
[48] Squires T M and Mason T G 2010 *Annu. Rev. Fluid Mech.* **42** 413
[49] Li Q, Peng X, Chen D and McKenna G B 2020 *Soft Matter* **16** 3378
[50] Evans R M L, Tassieri M, Auhl D and Waigh T A 2009 *Phys. Rev.* **80** 012501
[51] Bellour M, Skouri M, Munch J-P and Hébraud P 2002 *Eur. Phys. J.* E **8** 431
[52] Galvan-Miyoshi J M and Castillo R 2008 *Rev. Mex. Fis.* **54** 257
[53] Morales-Cruzado B, Delgado-Atencio J A, Vazquez-Montiel S and Sarmiento-Gómez E 2015 *Biomed. Opt. Express* **6** 1726
[54] van de Hulst H C 1980 *Multiple Light Scattering* vol 2 (New York: Academic)
[55] Hecht E 2002 *Optics* (Reading, MA: Addison-Wesley Developers Press)
[56] Kerker M 1969 *The Scattering of Light and Electromagnetic Radiation* (New York: Academic)
[57] Sarmiento-Gómez E, López-Díaz D and Castillo R 2010 *J. Phys. Chem.* B **114** 12193
[58] Tavera-Vázquez A, Arenas-Gómez B, Garza C, Liu Y and Castillo R 2018 *Soft Matter* **14** 7264
[59] López-Diaz D and Castillo R 2010 *J. Phys. Chem.* B **114** 8917
[60] Chu Z, Dreiss C A and Feng Y 2013 *Chem. Soc. Rev.* **42** 7174
[61] Rincón-Londoño N, Tavera-Vázquez A, Garza C, Esturau-Escofet N, Kozina A and Castillo R 2019 *J. Phys. Chem.* B **123** 9481
[62] Rincón-Londoño N, Garza C, Esturau-Escofet N, Kozina A and Castillo R 2021 *Colloids Surf.* A **610** 125903
[63] Oelschlaeger C, Schopferer M, Scheffold F and Willenbacher N 2009 *Langmuir* **25** 716